# Oxygen Vacancy Ordering and the Conductivity Maximum in Y_2O_3-Doped CeO_2

Mario Burbano,*[,†] Stefan T. Norberg,[‡,§] Stephen Hull,[§] Sten G. Eriksson,[‡] Dario Marrocchelli,[†,⊥] Paul A. Madden,[‖] and Graeme W. Watson*[,†]

[†]School of Chemistry and CRANN, Trinity College Dublin, College Green, Dublin 2, Ireland

[‡]Department of Chemical and Biological Engineering, Chalmers University of Technology, SE-41296 Gothenburg, Sweden

[§]The ISIS Facility, Rutherford Appleton Laboratory, Didcot, Oxfordshire, OX11 0QX, United Kingdom

[⊥]Department of Nuclear Science and Engineering, Massachusetts Institute of Technology, Cambridge, United States

[‖]Department of Materials, University of Oxford, Parks Road, Oxford OX1 3PH, United Kingdom

ABSTRACT: The defect structure and ionic diffusion processes within the anion-deficient, fluorite structured system $Ce_{1-x}Y_xO_{2-x/2}$ have been investigated at high temperatures (873 K−1073 K) as a function of dopant concentration, x, using a combination of neutron diffraction studies, impedance spectroscopy measurements, and molecular dynamics (MD) simulations using interionic potentials developed from ab initio calculations. Particular attention is paid to the short-range ion−ion correlations, with no strong evidence that the anion vacancies prefer, at high temperature, to reside in the vicinity of either cationic species. However, the vacancy−vacancy interactions play a more important role, with preferential ordering of vacancy pairs along the ⟨111⟩ directions, driven by their strong repulsion at closer distances, becoming dominant at high values of x. This effect explains the presence of a maximum in the ionic conductivity in the intermediate temperature range as a function of increasing x. The wider implications of these conclusions for understanding the structure−property relationships within anion-deficient fluorite structured oxides are briefly discussed, with reference to complementary studies of yttria and/or scandia doped zirconia published previously.

KEYWORDS: reverse Monte Carlo (RMC), molecular dynamics (MD), oxygen vacancy ordering, cation interactions, doped ceria (CeO₂), SOFC electrolytes
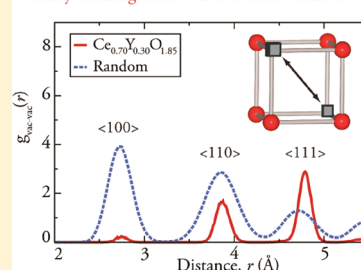
1. INTRODUCTION

Increasing environmental concerns regarding the long-term sustainability of current energy production methods have become a topic difficult to ignore. It is consequently important for the present and long-term viability of the world economy to find more efficient means to produce electricity. This includes an increased use of renewable energy sources, for example, solar cells and wind power, but also a much better use of existing carbon based fuels. Solid oxide fuel cells (SOFCs)[1−3] are one of the technologies that show most promise in this regard. One of the main benefits of this technology is the ability to use a variety of fuels, for example, natural gas, hydrogen, and gasified coal. In addition, SOFCs do not generate sulphurous, nitric, or hydrocarbon pollutants and have greatly reduced CO_2 emissions with respect to conventional energy generation systems. In contrast to heat engines, whose efficiency is limited by the Carnot cycle, SOFCs can achieve high fuel efficiencies (up to 85% for combined heat and power systems) by the direct electrochemical conversion of these fuels into electricity and heat.

Most modern SOFCs use Y_2O_3 doped ZrO_2 (yttria stabilized zirconia, YSZ, $Zr_{1-x}Y_xO_{2-x/2}$) as the electrolyte which transports oxide ions between the electrodes of the cell. YSZ is stabilized in the cubic fluorite structure (space group $Fm\overline{3}m$, Figure 1) by aliovalent doping with Y^{3+} ions, which substitute

Zr^{4+} ions on the face-centered cubic (fcc) cation lattice. Upon doping, charge compensating oxygen vacancies are formed in the anion sublattice, which facilitate oxide ion diffusion. However, this material has the drawbacks of undergoing temperature-dependent martensitic phase transformations and requiring high working temperatures (1073 K−1273 K), both of which place severe demands on the materials used for SOFC components, such as, the interconnect, cathode, anode, and solid electrolyte, because of the differential thermal expansion of these components and their corrosion at high temperatures. These operating conditions mean that conventional hydrocarbon fuels can be used without the need for expensive catalysts, but long start-up times are required. Doped cerias, $Ce_{1-x}M_xO_{2-x/2}$ with $M = Y^{3+}$, Gd^{3+}, and so forth,[4,5] also adopt the fluorite structure but possess a larger lattice parameter compared to YSZ, display higher ionic conductivities, and offer the possibility of operating SOFCs at intermediate temperatures (∼873−1073 K). These properties would make it possible to circumvent the above-mentioned drawbacks of current SOFC technologies and allow low chromium content
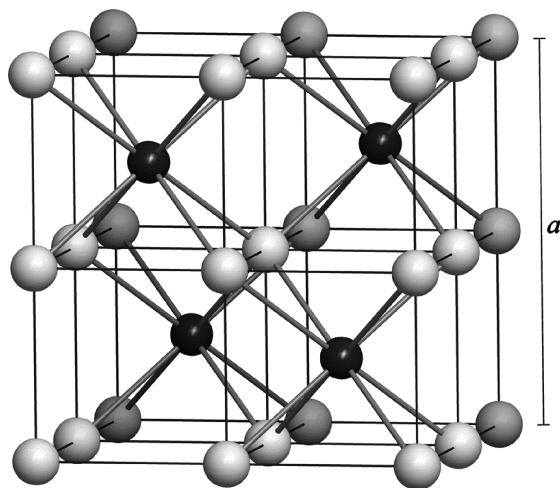
Figure 1. Cubic fluorite structure ($Fm\bar{3}m$) with cations (dark colored atoms) at the $4(a)$ sites at 0, 0, 0, etc. and the oxygen atoms at the $8(c)$ sites at 1/4, 1/4, 1/4, etc. The lattice parameter, a, is shown. Note that the figure is drawn in such a way that the cubic coordination around the cations is emphasized.

steels to be utilized thus reducing cathode degradation from chrome poisoning.[6,7]

Recently, an extensive examination of the factors which influence the mobility of the oxygen anion vacancies in YSZ and the closely related scandia stabilized zirconia (ScSZ, $Zr_{1-x}Sc_xO_{2-x/2}$) was completed using a combination of reverse Monte Carlo (RMC) analyzed neutron diffraction, conductivity measurements and molecular dynamics (MD) simulation.[8,9] These studies found that vacancy mobility in an aliovalently doped fluorite-structured material is limited by short-range vacancy ordering effects. At low concentrations, the ordering is driven by the substitutional disorder on the cation sublattice (cation-vacancy ordering), with the vacancies tending to lie in the first coordination shell of the smaller cation. For this reason ScSZ has a higher conductivity than YSZ because the Sc^{3+} cation has a very similar size to the Zr^{4+} host, whereas Y^{3+} is substantially larger. At higher dopant concentrations, vacancy–vacancy ordering effects become dominant and limit the extent to which the conductivity of a given material can be increased simply by increasing the number of vacancies (i.e., increasing x). In practice, the maximum conductivity for YSZ is reached at $x \sim 0.16$.[10,11] The extent to which the full x-dependence of the conductivity can be mapped out in ZrO_2-based materials is limited because at relatively low x-values they transform into nonfluorite structured phases with tetragonal and monoclinic symmetry. On the other hand, yttria-doped ceria, YDC, maintains the fluorite structure for all relevant dopant concentrations and, because the size of the Y^{3+} cation is very similar to that of Ce^{4+}, the cation-vacancy ordering effects should be smaller than those observed in YSZ. It is generally assumed that the vacancies are isolated and randomly distributed over the anion sublattice at low dopant concentrations. However, at higher levels the ionic conductivity falls as the vacancies tend to become trapped in defect clusters, thus limiting the number of effective charge carriers. In the case of undoped $CeO_{2-\delta}$, neutron diffraction studies, under variable atmospheres down to $\delta = 0.290(8)$, showed that the vacancies preferentially align as pairs in $\langle 111 \rangle$ directions[12] so that, on a local scale, the structure resembles that of the vacancy ordered compound Ce_7O_{12} ($\delta = 0.286$) under ambient conditions.[13]

This work examines the factors that affect the ionic conductivity of YDC at its working temperature as an electrolyte in SOFC applications. In particular, we investigate the effect of oxygen vacancy ordering on the conductivity of YDC using a combination of experimental neutron diffraction, ionic conductivity data, and molecular dynamics simulations, with a newly parametrized DIPole Polarizable Ion Model (DIPPIM) potential.[14]

2. EXPERIMENTS

2.1. Sample Preparation. Powder samples of $Ce_{1-x}Y_xO_{2-x/2}$ with $x = 0.04, 0.08, 0.11, 0.18,$ and 0.26 (corresponding to 2, 4, 6, 10, and 15 mol % Y_2O_3), of typical volumes of 2.5 cm^3 were prepared by mixing stoichiometric amounts of the previously dried binary oxides CeO_2 and Y_2O_3 supplied by the Aldrich Chemical Co. and of stated purities 99.995% and 99.99%, respectively. Each sample mixture was thoroughly ground for about 1 h and heated to 1823 K for 24 h before being pressed into pellets that were then heated for another 48 h at 1823 K. Samples used for neutron diffraction were subsequently crushed and ground into a fine homogeneous powder. After the neutron diffraction experiment the samples were resintered to pellets at 1773 K and used for the impedance spectroscopy studies.

2.2. Impedance Spectroscopy. The total (bulk plus grain boundary) ionic conductivity of the prepared $Ce_{1-x}Y_xO_{2-x/2}$ samples was measured on sample pellets of approximately 10 mm diameter and 1 mm height using platinum electrodes and a voltage of 1 V. Platinum paste was used to ensure good contact between the electrodes and the sample. The samples were then heated to 1473 K in air, and the complex impedance spectroscopy was performed during cooling at 10 K intervals, using a Solartron SI 1260 Frequency Response Analyzer over a frequency range from 1 Hz to 1 MHz. The total conductivity was determined by least-squares equivalent circuit fitting to the frequency dependent impedance data using the program ZVIEW.

2.3. Neutron Powder Diffraction. Neutron diffraction data was collected at the Polaris diffractometer of the ISIS facility, Rutherford Appleton Laboratory, U.K.,[15] using the backscattering detector bank (covering scattering angles of $130° < 2\theta < 160°$), the $\sim90°$ detector bank ($85° < 2\theta < 95°$), and the low angle detector bank ($28° < 2\theta < 42°$). These detector banks cover an approximate range of scattering vectors Q (where $Q = 2\pi/d$ and d is the interplanar spacing) of 2−40 Å^{-1}, 1.5−20 Å^{-1}, and 0.8−12 Å^{-1}, respectively. Each powder sample was measured at 1073 K while encapsulated in a cylindrical quartz tube with a 10 mm inner diameter and a 0.5 mm wall thickness. The furnace used is designed for neutron scattering experiments and employs vanadium as heating elements and heat shields. The setup allowed for an open air inlet to the powder sample which removes any possibility of reducing Ce^{4+} to Ce^{3+} at the measured temperatures. Each measurement took approximately 12 h to obtain counting statistics of sufficient quality to allow analysis of the total (Bragg plus diffuse scattering components) scattering. Preliminary Rietveld analysis of the averaged structures using only the Bragg scattering was performed using the GSAS software.[16]

2.4. Neutron Total Scattering. The diffraction data from each detector bank for each sample were corrected for the effects of background scattering and beam attenuation, and subsequently merged to a single spectrum covering a wide Q range using the program Gudrun.[17] This process puts the scattered intensity onto an absolute scale of scattering cross-section. The resultant normalized total scattering structure factor, $S(Q)$, was used to generate the corresponding total radial distribution function (RDF), $G(r)$, via a Fourier transform

$$G(r) = \frac{1}{(2\pi)^3 \rho_0} \int_0^\infty 4\pi Q^2 \, S(Q) \frac{\sin Qr}{Qr} dQ \tag{1}$$

where ρ_0 is the average atom number density in atoms Å^{-3} (for details, see Keen[18]).

The $G(r)$ can also be expressed in terms of the individual partial RDFs, $g_{ij}(r)$, weighted by the concentrations of the two species, c_i and

c_j, and their coherent bound neutron scattering lengths, $\bar{b}_i$ and $\bar{b}_j$, so that

$$G(r) = \frac{\sum_{i,j=1}^{n} c_i c_j \bar{b}_i \bar{b}_j \, g_{ij}(r)}{\sum_{i=1}^{n} (c_i \bar{b}_i)^2} \tag{2}$$

where n is the number of ionic species. The partial RDF is in turn given by

$$g_{ij}(r) = \frac{1}{4\pi r^2 \mathrm{d}r} \frac{n_{ij}(r)}{\rho_j} \tag{3}$$

with $n_{ij}(r)$ equal to the number of atoms of type j located at a distance between r and $r + \Delta r$ from an atom of type i and ρ_j is the number density of atoms of type j, given by $\rho_j = c_j \rho_0$. These individual partial distribution functions, $g_{ij}(r)$, can be obtained from RMC modeling, which simultaneously probes both the long- and the short-range structural properties of the system.

2.5. RMC Modeling Details. All RMC analyses[19] of the neutron total scattering data (Bragg peaks plus diffuse scattering components) were performed using the RMCProfile software.[20] Each RMC model, one for each sample stoichiometry, used a configuration box of 10 × 10 × 10 unit cells. This gives a total of 4000 cations, Ce^{4+} and Y^{3+}, in their given stoichiometric ratio and a corresponding number of O^{2-} anions required to charge balance the cells; their numbers varied from 7920 ($x = 0.039$) and 7480 ($x = 0.261$). The starting models had all the cations randomly distributed over their regular crystallographic positions, and likewise the oxygen vacancies were randomly distributed over the oxygen sites. A soft bond valence sum (BVS) constraint[21] was used to keep individual cation–anion surroundings chemically reasonable, and all BVS parameters were taken from Brese and O'Keeffe.[22]

Note that in all cases the RMC modeling was fitted against reciprocal space data, $S(Q)$, real space data, $G(r)$, as well as the Bragg profile data. The latter provides the constraint of long-range crystallinity, while the $S(Q)$ emphasizes the long-range ordering and the $G(r)$ focuses on the short-range interactions. Additionally, the $S(Q)$ is broadened by convolution with a box function to reflect the finite size of the configuration box (for details, see Tucker et al.[20]).

2.6. Interionic Potential. The interaction potential used in this study is known as the DIpole Polarizable Ion Model (DIPPIM). This model allows the ionic species to carry their formal valence charges (Ce^{4+}, Y^{3+}, and O^{2-}) and accounts for polarization effects resulting from the induction of dipoles on the ions. This potential model has been validated in several studies of oxide systems.[23−28] While a number of different potential models exist and have been applied to ceria,[29,30] our DIPPIM model uses parameters optimized directly from state-of-the-art density functional theory (DFT) calculations from which detailed information about the forces and dipoles can be extracted. In contrast, shell model potentials are usually parametrized to reproduce empirical results such as high-pressure structural data or phonon dispersion curves.[30] The details of the parameter optimization procedure, for this and other DIPPIM potentials, have been described elsewhere by authors of this article.[14,25,28] The potential parameters used in this study are reported in Table 1.

2.7. MD Simulation Details. All molecular dynamics simulations on the cubic $Ce_{1-x}Y_xO_{2-x/2}$ system were performed using a supercell of 4 × 4 × 4 unit cells for a range of x values (Table 2). Each model was set up by distributing the ions randomly over their average crystallographic positions, as for the RMC modeling. Coulombic and dispersion interactions were summed using Ewald summations,[31] while the short-range part of the potential was truncated to half the length of the simulation box (~10 Å). Each concentration was initially equilibrated at a temperature of 2073 K for 120 ps; the temperature was then scaled down to room temperature at a rate of 1.64 K ps^{-1}. The diffusion coefficients were calculated for temperatures of 873 K and above. All simulations were performed at constant temperature and pressure (NPT ensemble), as described by Martyna et al.,[32] using a time step of 1 fs. In addition to these calculations, we also constructed model systems (referred to as average cation ac-YDC) where

Table 1. Parameters for the DIPPIM Potential with Values Given in a.u.[a]

	Repulsive and Dispersion Parts		
	O–O	Y–O	Ce–O
A^{ij}	55.3	111.1	105.9
a^{ij}	6.78	1.377	1.269
B^{ij}	50000	50000	50000
b^{ij}	0.85	1.35	1.40
C_6^{ij}	53	12	12
C_8^{ij}	1023	240	240
b_{disp}^{ij}	1.0	1.5	1.5
	Polarizabilities and Damping Parameters		
α	14.9	2.60	5.0
b_D^{O-O}	1.73	c_D^{O-O}	0.45
b_D^{O-Y}	1.68	c_D^{O-Y}	1.62
b_D^{O-Ce}	1.76	b_D^{O-Ce}	1.93
b_D^{Y-O}	1.68	c_D^{Y-O}	−0.95
b_D^{Y-Y}	0.59	b_D^{Y-Y}	−0.33
b_D^{Y-Ce}	0.75	b_D^{Y-Ce}	−0.46
b_D^{Ce-O}	1.76	c_D^{Ce-O}	−0.47
b_D^{Ce-Y}	0.75	c_D^{Ce-Y}	−0.37
b_D^{Ce-Ce}	1.07	c_D^{Ce-Ce}	−0.84

[a]Only those short-range parameters not equal to zero are reported. See Norberg et al.[27] for further information concerning the DIPPIM potential parameters.

Table 2. Atomic Compositions Used in the MD Simulations

x	no. of Ce^{4+} ions	no. of Y^{3+} ions	no. of O^{2-} ions	no. of vacancies
0	256	0	512	0
0.039	246	10	507	5
0.078	236	20	502	10
0.117	226	30	497	15
0.179	210	46	489	23
0.203	204	52	486	26
0.242	194	62	481	31
0.257	190	66	479	33
0.304	178	78	473	39
0.360	164	92	466	46
0.406	152	104	460	52

both cations are assigned the same short-range potential parameters as those of the Ce^{4+} ions in the original potential. In this model both cations are given the same charge so that the total for all cations balances that of the O^{2-} ions present in the simulation for the same concentration ranges that were used in the calculations described above for $Ce_{1-x}Y_xO_{2-x/2}$. These idealized systems allow us to eliminate the effects of differing charges and lattice strain induced by having both host and dopant cations and serve as reference systems in which the cation-vacancy ordering effects are absent. All these calculations were performed with an in-house code called PIMAIM.

3. RESULTS AND DISCUSSION

3.1. Rietveld Analysis. An average structure model for each sample was refined with the Rietveld method[33] using the GSAS software.[16] The structure models were based on the fluorite type structure with Ce^{4+} and Y^{3+} randomly arranged over the fcc lattice ($m3m$ symmetry at site 0, 0, 0, etc.) and oxygen randomly positioned in the tetrahedral holes ($\overline{4}3m$ symmetry at site 1/4, 1/4, 1/4, etc.) according to the sample stoichiometry. The refined parameters consisted of a scale

factor, cubic lattice parameter a, isotropic thermal vibration parameters for the cations and anions, 18 coefficients of a shifted Chebyshev polynomial to describe the undulating background scattering caused by the sample container, and 4 coefficients describing Gaussian and Lorentzian contributions to the Bragg peak profile shape. The collected data used for the Rietveld refinement covered a d-spacing from ∼3.2 to 0.33 Å, and excellent fits were obtained for all samples, see Table 3 for crystallographic parameters, with the final weighted R-factors between 0.81% and 1.50% using 4404 data points.

Table 3. Rietveld Refinement of $Ce_{1-x}Y_xO_{2-x/2}$ Samples at 1073 K

sample	lattice parameter	U_{iso} cations	U_{iso} anions
$Ce_{0.96}Y_{0.04}O_{1.98}$	5.468743(14)	0.01256(10)	0.02128(8)
$Ce_{0.92}Y_{0.08}O_{1.96}$	5.463202(14)	0.01348(11)	0.02228(9)
$Ce_{0.89}Y_{0.11}O_{1.95}$	5.470539(15)	0.01444(11)	0.02334(9)
$Ce_{0.82}Y_{0.18}O_{1.91}$	5.454229(14)	0.01650(13)	0.02622(11)
$Ce_{0.74}Y_{0.26}O_{1.87}$	5.470301(19)	0.01956(16)	0.03015(16)

The thermal vibration parameters follow the expected trend of increasing amplitudes with increased concentration of oxygen vacancies. However, the lattice parameter shows no systematic trend with dopant level, because of unavoidable shifts in the sample positioning between data collections using different samples. This is confirmed by a lack of consistency between lattice parameter values obtained by analysis of data collected in different portions of the detector banks. The possibility that the anomalous behavior arises from reduction of a fraction of the Ce^{4+} to Ce^{3+} within some of the samples can be excluded, since allowing the mean occupancy of the anion sites to vary within the refinements[12] gave values consistent (within error) with those expected purely for doping of Ce^{4+} sites with Y^{3+}. Results from the Rietveld refinements, that is, peak profile information, background parameters, and instrument parameters, were used in the RMC modeling. These results are presented in next section.

3.2. RMC results. The RMC modeling generated configuration boxes whose calculated $G(r)$, $S(Q)$, and Bragg patterns agreed extremely well with the experimental data. Figure 2 shows the fits for the $Ce_{0.739}Y_{0.261}O_{1.870}$ sample which contains the highest oxygen vacancy concentration and consequently has the most locally disordered structure. It is additionally possible to extract partial RDFs from the RMC configuration boxes, and this information has been used together with experimental data to validate the MD simulations.

3.3. MD Structure Analysis. Figure 3 shows the change in cubic lattice parameter, a, at 300 K as a function of dopant concentration in $Ce_{1-x}Y_xO_{2-x/2}$, obtained from the MD simulations (blue squares) and from previous XRD experiments (red diamonds and black circles[34,35]). The trend observed is that the lattice constant decreases as the dopant concentration increases. This is caused by vacancy formation upon doping, which counteracts the increased number of the slightly larger Y^{3+} cations. This effect is discussed in detail in ref 36. The simulated lattice parameters are not compared to the experimental results from this work for the reason outlined in section 3.1. Figure 4 compares the total RDF, $G(r)$, generated from the MD simulations (using eq 2) with those obtained from the neutron diffraction experiments, both at 1073 K and represented by red dashed lines and black solid lines, respectively. The range of concentrations shown is from $x = 0.04-0.26$. In addition, the results for a 10 ps Local Density Approximation
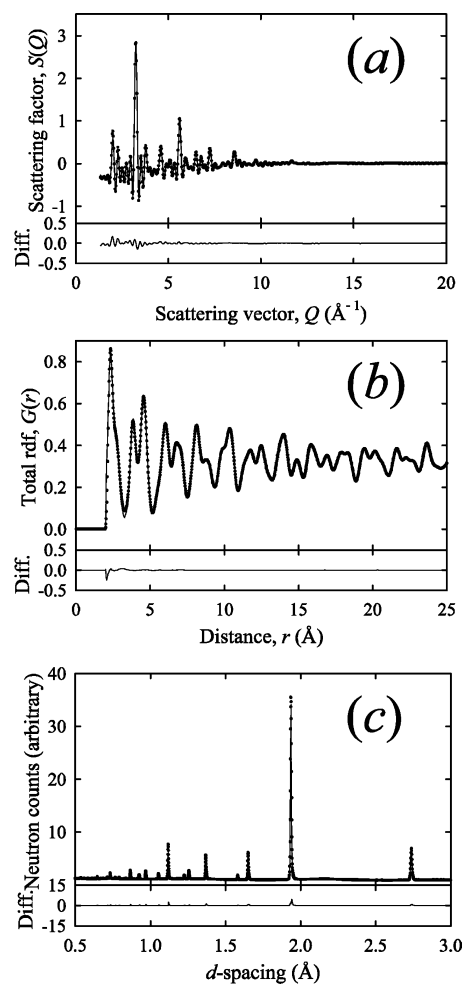

Figure 2. Fits to (a) $S(Q)$, (b) $G(r)$, and (c) the Bragg scattering profile obtained by RMC modeling for $Ce_{0.739}Y_{0.261}O_{1.870}$ at 1073 K. The dots show the experimental data, and the solid lines show the calculated profiles. The lower traces illustrate the difference between the experimental and fitted profiles.
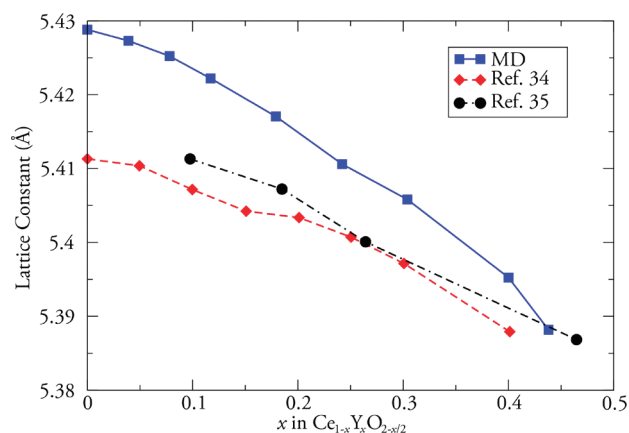

Figure 3. Room temperature experimental (red diamonds and black circles), taken from previously published XRD data,[34,35] and DIPPIM (blue squares) lattice constants as a function of dopant concentration x in $Ce_{1-x}Y_xO_{2-x/2}$.

(LDA) Car–Parrinello MD[37] simulation performed for the composition $x = 0.12$, shows the high level of agreement between our interatomic potential and ab initio. Overall, the agreement between the MD simulations and the neutron
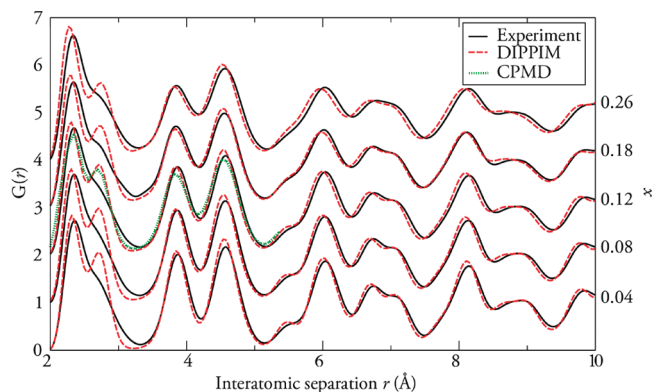
Figure 4. Total distribution functions $G(r)$ for x = 0.04, 0.08, 0.12, 0.18, and 0.26 from experiment (black solid lines) and MD (red dashed lines). The green dotted line represents a Car−Parrinello MD simulation for x = 0.12.

diffraction data in Figure 4 is good, the only deviation (common to both MD and ab initio simulations) being that the simulated peak at around 2.7 Å is slightly sharper that the experimental one.

Figure 5 shows a plot of the partial RDFs, $g_{ij}(r)$, for $Ce_{0.88}Y_{0.12}O_{1.94}$ at 1073 K, from MD, RMC, and ab initio simulations.
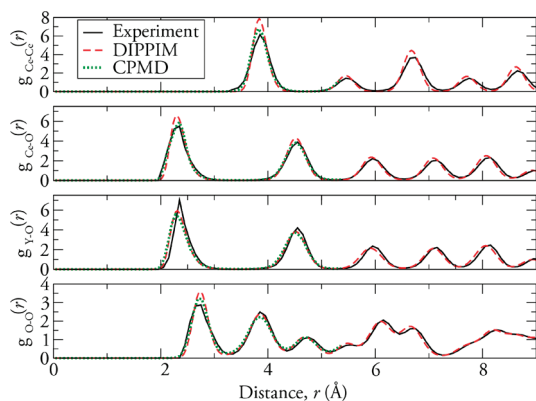

Figure 5. Partial distribution functions, $g_{ij}(r)$, from MD simulations (red dashed lines) and experiment (black solid lines) for $Ce_{0.88}Y_{0.12}O_{1.94}$. The green dotted lines represent a Car−Parrinello MD simulation for x = 0.12.

Overall, the high level of agreement between the data sets confirms that the DIPPIM potential used here is able to account well for the structural properties of YDC at various dopant concentrations. The plots for $g_{Ce-O}(r)$ and $g_{Y-O}(r)$ show that the Y−O distance is slightly longer than Ce−O, which is explained by the stronger Coulombic attraction exerted by the Ce^{4+} cation and is in good agreement with Shannon's radii of 0.97 Å and 1.019 Å for Ce^{4+} and Y^{3+}, respectively.[38] Overall, this comparison shows that the DIPPIM potential can satisfactorily reproduce the experimental structural data for this system. In the next section, we will therefore focus on cation−vacancy and vacancy−vacancy ordering tendencies (which can be probed only with computer simulations) and their effects on the conductivity of this material.

3.4. Cation-Vacancy Interactions. The vacancy ordering analysis was performed by specifying the tetrahedra formed by the cations coordinated to the anion sites in the fluorite structure. Thus, for a given instantaneous ionic configuration it is

possible to determine which of these sites are empty at a given time during a simulation. It is important to distinguish between instances where a given site is truly vacant and those in which an oxide-ion temporarily leaves the cavity because of thermal vibrations. These considerations have been examined in detail elsewhere.[9,36] The vacancy positions were then used to calculate RDFs, which allowed the study of vacancy ordering in real space.

Figure 6 shows the $g_{cat-vac}(r)$ at 1073 K for x = 0.18 (a), 0.26 (b), 0.30 (c), and 0.36 (d) in $Ce_{1-x}Y_xO_{2-x/2}$. The first two
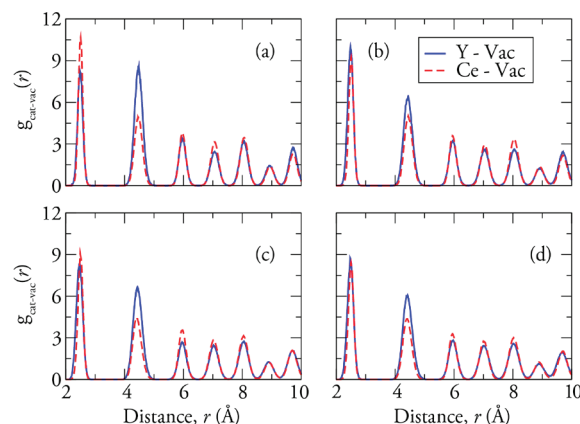

Figure 6. Cation-vacancy partial distribution functions, $g_{cat-vac}(r)$, obtained from MD simulations at 1073 K for x = 0.18 (a), 0.26 (b), 0.30 (c), and 0.36 (d) in $Ce_{1-x}Y_xO_{2-x/2}$. Y-vacancy and Ce-vacancy $g(r)$'s are represented by blue (solid) lines and red (dashed) lines, respectively.

peaks in the RDFs represent the number of vacancies that are in the nearest neighbor and next-nearest neighbor position of each cation, respectively. The results show that there is no clear tendency for the vacancies to associate with either cation at the nearest neighbor position, although the next nearest neighbor position shows, especially for low dopant concentrations, enhanced association of the vacancies with the Y^{3+} cations with respect to the Ce^{4+} cations, which indicates repulsion of the vacancies by the former species.

At first, our results might seem at odds with previous evidence from the literature. Indeed, room temperature MAS NMR measurements on YDC show clearly that the Y coordination number is smaller than that of the Ce cations, thus implying that vacancies associate with Y cations.[35,39] Static calculations, based on interatomic potentials or DFT, also show that there is a preference for vacancies to be nearest-neighbor to Y, as opposed to next nearest neighbor. However, this preference is rather weak, and the energy difference between these two configurations is smaller than 0.1−0.2 eV.[35,39] This explains why we do not observe such ordering in our simulations. Indeed, since our calculations are performed at high temperatures (>873 K), this weak ordering tendency is washed out by entropic effects. This argument is confirmed by recent calorimetric measurements, performed at 973 K, which show that little defect ordering is observed in YDC compared to YSZ and yttria-doped HfO_2. Kim et al.[35] performed ^{17}O MAS NMR studies and found evidence of different resonances, which they assigned to oxygen atoms with different numbers of yttrium cations in the first coordination sphere. However, when the temperature is raised to 673 K, these resonances coalesce, indicating that at this temperature this ordering effect vanishes.

3.5. Vacancy−Vacancy ordering. Figure 7 illustrates the $g_{vac\text{-}vac}(r)$ at a range of dopant concentrations at 1073 K. For the
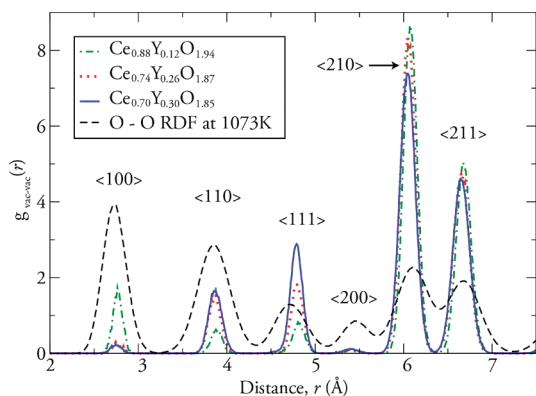

Figure 7. Vacancy−vacancy partial RDF, $g_{vac\text{-}vac}(r)$, obtained from MD simulations at 1073 K for $x = 0.12$, 0.26, 0.30 in $Ce_{1-x}Y_xO_{2-x/2}$.

purpose of comparison, a $g_{O\text{-}O}(r)$ for CeO_2 at the same temperature is also included as it represents that expected from a random distribution of vacancies. The directions/distances in the simple cubic oxygen sublattice are indicated by $\langle 100 \rangle$, $\langle 110 \rangle$, $\langle 111 \rangle$, $\langle 200 \rangle$, and so forth. The patterns observed indicate that there is an enhanced ordering of oxygen vacancies along the $\langle 210 \rangle$ and $\langle 211 \rangle$ directions that is not dependent on the dopant concentration. Figure 7 also indicates that as the Y^{3+} content increases the vacancies tend to pair along the $\langle 111 \rangle$ direction with respect to the random distribution. This has been observed in several fluorite structured oxides.[8,9,12]

3.6. Ionic Conductivity. The ionic conductivity was estimated from the MD simulations using the Nernst−Einstein formula

$$\sigma_{NE} = \frac{c^2 \rho D}{k_B T} \tag{4}$$

where c is the charge of the mobile species, ρ is the system density, D is the diffusion coefficient, k_B is the Boltzmann constant, and T is the temperature. The diffusion coefficient, D, can be calculated from the slope of the mean square displacement of individual ions versus time at long times, that is,

$$D = \lim_{t \to \infty} \frac{1}{6N} \langle \sum_{f=1}^{N} [r_j(t) - r_j(0)]^2 \rangle \tag{5}$$

Figure 8 shows the ionic conductivity as a function of dopant concentration at 1073 and 873 K obtained from experiment and simulations. At the temperatures in question there is a peak in the conductivity (σ) with increasing Y^{3+} content at $x \sim 0.12$ for the experimental data. This maximum is less pronounced in the MD simulation data, possibly because of the relatively small system sizes studied in this work, but it also occurs at $x \sim 0.12$ in the case of the 1073 K simulations. This peak becomes less pronounced at 873 K for both data sets. These data are in excellent agreement with those reported elsewhere and highlight the predictive capabilities of the DIPPIM potential.[40] We have also reported, in a previous article,[14] that the oxygen migration energy obtained for YDC from MD calculations compares well with experimental and simulation data in the literature for this temperature range.[41−43]
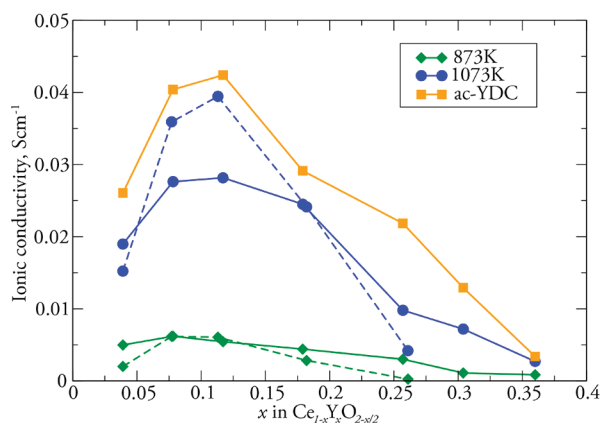

Figure 8. Ionic conductivity as a function of dopant concentration at 1073 K (blue lines with circles) and 873 K (green lines with diamonds). Dashed and solid lines represent experimental and MD results, respectively. The orange line with squares corresponds to the conductivity at 1073 K of the average cation systems (ac-YDC) where the cations carry the same charge.

As discussed above, the shape of the conductivity versus composition plot is usually attributed to two types of interactions, namely, those between cations and vacancies and those between vacancies themselves. Our study of these interactions has shown no clear evidence for the former, but a strong tendency for vacancies to pair along the $\langle 111 \rangle$ direction with increasing dopant concentration. To confirm which of these effects dominates the observed maximum in conductivity, we also show in Figure 8 a plot of the conductivities at 1073 K for the average cation systems, ac-YDC, where both cationic species carry the same charge and have the same short-range repulsion interactions with the oxide ions. These calculations were included to explore the effects of the vacancy−vacancy interaction in a more direct manner, given that cation−vacancy effects are, *de facto*, eliminated in ac-YDC. In this case we see that the conductivity has a peak at the same dopant concentration, although all values are higher than either the experimental or the simulated results for the real system at the same temperature. The latter is probably a consequence of the potential which has, on average, less repulsive short-range interactions.[9] Figure 8 shows that, even if all the differences between the cation species are removed, a maximum in the conductivity is still observed in ac-YDC, which happens at the same vacancy concentration as in the real material, $x = 0.12$. This serves to confirm that *the observed maximum in the conductivity, and its subsequent drop, are predominantly caused by vacancy−vacancy interactions.* In addition, we also examined the $g_{vac\text{-}vac}(r)$ for the ac-YDC systems (not shown) and found that they displayed the same vacancy ordering patterns as those shown in Figure 7.

4. CONCLUSIONS

This study has assessed the role of two processes which affect the conductivity in $Ce_{1-x}Y_xO_{2-x/2}$ (YDC), namely, the local ordering of the anion vacancies and their preference to reside in the vicinity of either cationic species. The former was found to have a more pronounced effect with increasing x, while there was no clear tendency for the vacancies to be located near the host Ce^{4+} or dopant Y^{3+} cations in the intermediate temperature range. In fact, it was found that vacancy ordering along the $\langle 111 \rangle$ direction, driven by their strong repulsion at closer distances,[44,45] dominates at high x values. The decreasing ionic

conductivity with increasing x is, therefore, for the most part dominated by vacancy—vacancy interactions in YDC. This was confirmed by performing simulations on average cation, ac-YDC, systems, where both cationic species carry the same charge and have the same short-range repulsion interactions with the oxide ions. Our results showed that the ac-YDC systems displayed the same maximum in conductivity as those where the ions carry their formal charges, namely $x \sim 0.12$.

In our previous work, we studied the local ordering of anion vacancies in a series of fluorite-structured materials such as YSZ, ScSZ, $CeO_{2-\delta}$, $Zr_{0.5-0.5x}Y_{0.5+0.25x}Nb_{0.25x}O_{1.75}$,[8,9,12,46] by using complementary information provided by key experimental (neutron diffraction studies coupled with a RMC analysis and impedance spectroscopy measurements) and computational (ab initio based MD simulations) techniques. For all compounds a strong ordering of the vacancies along $\langle 111 \rangle$ directions were found together with a preference for the vacancies to reside in the vicinity of the smaller cationic species—when these have ionic radii that are quite different, such as the case of YSZ.

This report finds that the same arguments apply to YDC. As result of this, we conclude that the vacancy ordering tendencies in these fluorite-structured materials are very similar and share the same features, even though the local structure of these materials can be very different.[9,12,27,28] Most importantly, the tendency for vacancies to order along the $\langle 111 \rangle$ direction is found to be little influenced by either the dopant or the host cation species, and this tendency is still observed even when the differences between the host and the dopant cations are completely removed. This study would therefore appear to confirm our previous hypothesis that vacancy—vacancy interactions in these materials are an intrinsic effect, rather like a "property" of the fluorite lattice, and that, consequently, they cannot be minimized/avoided by changing the chemistry of these compounds[50]. This has significant consequences as these interactions ultimately limit the conductivity of these materials for $x > 0.12$. For these reasons, we recommend that the quest for candidate solid electrolyte materials with significantly improved characteristics for future SOFCs should concentrate either on other systems or on different optimization strategies, such as YSZ or YDC heterostructures.

■ AUTHOR INFORMATION

Corresponding Author
*E-mail: burbanom@tcd.ie (M.B.), watsong@tcd.ie (G.W.W.).

■ ACKNOWLEDGMENTS

■ REFERENCES

(1) Stambouli, A. B.; Traversa, E. *Renewable Sustainable Energy Rev.* **2002**, *6*, 433−455.

(2) Badwal, S. P. S; Foger, K. *Ceram. Int.* **1996**, *22*, 257−265.

(3) Brandon, N. P.; Skinner, S.; Steele, B. C. H. *Annu. Rev. Mater. Res.* **2003**, *33*, 183−213.

(4) Andersson, D. A.; Simak, S. I.; Skorodumova, N. V.; Abrikosov, I. A.; Johansson, B. *Proc. Natl. Acad. Sci. U.S.A.* **2006**, *103*, 3518−3521.

(5) Tuller, H. L.; Nowick, A. S. *J. Electrochem. Soc.* **1975**, *122*, 255−259.

(6) Jiang, S. P.; Zhen, Y. *Solid State Ionics* **2008**, *179*, 1459−1464.

(7) Yang, Z.; Fergus, J. W. In *Green Chemistry and Chemical Engineering*; CRC Press: Boca Raton, FL, 2008; pp 179−212.

(8) Norberg, S. T.; Hull, S.; Ahmed, I; Eriksson, S. G.; Marrocchelli, D.; Madden, P. A.; Li, P.; Irvine, J. T. S. *Chem. Mater.* **2011**, *23*, 1356−1364.

(9) Marrocchelli, D.; Madden, P. A.; Norberg, S. T.; Hull, S. *Chem. Mater.* **2011**, *23*, 1365−1373.

(10) Subbarao, E. C.; Ramakrishnan, T. V. *Fast Ion Transport in Solids*; Elsevier/North-Holland: New York, 1979.

(11) Nakamura, A.; Wagner, J. J. B. *J. Electrochem. Soc.* **1986**, *133*, 1542−1548.

(12) Hull, S.; Norberg, S. T.; Ahmed, I.; Eriksson, S. G.; Marrocchelli, D.; Madden, P. A. *J. Solid State Chem.* **2009**, *182*, 2815−2821.

(13) Kümmerle, E. A.; Heger, G. *J. Solid State Chem.* **1999**, *147*, 485−500.

(14) Burbano, M.; Marrocchelli, D.; Yildiz, B.; Tuller, H. L.; Norberg, S. T.; Hull, S.; Madden, P. A.; Watson, G. W. *J. Phys.: Condens. Matter* **2011**, *23*, 255402.

(15) Hull, S.; Smith, R. I.; David, W. I. F.; Hannon, A. C.; Mayers, J.; Cywinski, R. *Phys. B: (Amsterdam, Neth.)* **1992**, *180−181* (Part 2), 1000−1002.

(16) Larson, A. C.; R. B. Von Dreele. *General Structure Analysis System (GSAS)*; Los Alamos National Laboratory: Los Alamos, NM, 1994.

(17) Soper, A. K. *Gudrun - A computer program developed for analysis of neutron diffraction data*; http://www.isis.stfc.ac.uk/groups/disordered-materials/software/, 2010.

(18) Keen, D. A. *J. Appl. Crystallogr.* **2001**, *34*, 172−177.

(19) McGreevy, R. L. *J. Phys.: Condens. Matter* **2001**, *13*, R877.

(20) Tucker, M. G.; Keen, D. A.; Dove, M. T.; Goodwin, A. L.; Hui, Q. *J. Phys.: Condens. Matter* **2007**, *19*, 335218.

(21) Norberg, S. T.; Tucker, M. G.; Stephen, H. *J. Appl. Crystallogr.* **2009**, *42*, 179−184.

(22) Brese, N. E.; O'Keeffe, M. *AcCrB* **1991**, *47*, 192−197.

(23) Wilson, M.; Jahn, S.; P.A., M. *J. Phys.: Condens. Matter* **2004**, *16*, S2795−S2810.

(24) Marrocchelli, D.; Salanne, M.; Madden, P. A.; Simon, C.; Turq, P. *Mol. Phys.* **2009**, *107*, 443−452.

(25) Madden, P. A.; Heaton, R.; Aguado, A.; Jahn, S. *J. Mol. Struct.: THEOCHEM* **2006**, *771*, 9−18.

(26) Marrocchelli, D.; Salanne, M.; Madden, P. A. *J. Phys.: Condens. Matter* **2010**, *22*, 152102.

(27) Norberg, S. T.; Ahmed, I; Hull, S.; Marrocchelli, D.; Madden, P. A. *J. Phys.: Condens. Matter* **2009**, *21*, 215401.

(28) Marrocchelli, D.; Madden, P. A.; Norberg, S. T.; Hull, S. *J. Phys.: Condens. Matter* **2009**, *21*, 405403.

(29) Lewis, G. V.; Catlow, C. R. A. *J. Phys. C: Solid State Phys.* **1985**, *18*, 1149.

(30) Catlow, C. R. A.; Guo, Z. X.; Miskufova, M.; Shevlin, S. A.; Smith, A. G. H.; Sokol, A. A.; Walsh, A.; Wilson, D. J.; Woodley, S. M. *Phil. Trans. R. Soc. A* **2010**, *368*, 3379−3456.

(31) Ewald, P. P. *AnP* **1921**, *369*, 253−287.

(32) Martyna, G. J.; Tobias, D. J.; Klein, M. L. *J. Chem. Phys.* **1994**, *101*, 4177−4189.

(33) Rietveld, H. *J. Appl. Crystallogr.* **1969**, *2*, 65−71.

(34) Zhang, T. S.; Ma, J.; Huang, H. T.; Hing, P.; Xia, Z. T.; Chan, S. H.; Kilner, J. A. *Solid State Sci.* **2003**, *5*, 1505−1511.

(35) Kim, N.; Stebbins, J. F. *Chem. Mater.* **2007**, *19*, 5742−5747.

(36) Marrocchelli, D.; Bishop, S.; Tuller, H. L.; Yildiz, B. *Adv. Funct. Mater.* **2011**.

(37) Car, R.; Parrinello, M. *Phys. Rev. Lett.* **1985**, *55*, 2471−2474.

228

dx.doi.org/10.1021/cm2031152 | *Chem. Mater.* 2012, 24, 222−229

(38) Shannon, R. D. *Acta Crystallogr., Sect. A* **1976**, *32*, 155−169.

(39) Maekawa, H.; Kawata, K.; Xiong, Y. P.; Sakai, N.; Yokokawa, H. *Solid State Ionics* **2009**, *180*, 314−319.

(40) Balazs, G. B.; Glass, R. S. *Solid State Ionics* **1995**, *76*, 155−162.

(41) Steele, B. C. H.; Floyd, J. M. *Proc. Br. Ceram. Soc.* **1971**, *19*, 55.

(42) Tuller, H. L.; Nowick, A. S. *J. Phys. Chem. Solids* **1977**, *38*, 859−867.

(43) Dholabhai, P. P.; Adams, J. B.; Crozier, P.; Sharma, R. *J. Chem. Phys.* **2010**, *132*, 094104.

(44) Bogicevic, A.; Wolverton, C. *Phys. Rev. B* **2003**, *67*, 024106.

(45) Pietrucci, F.; Bernasconi, M.; Laio, A.; Parrinello, M. *Phys. Rev. B* **2008**, *78*, 094301.

(46) Marrocchelli, D.; Madden, P. A.; Norberg, S. T.; H. S.. In *Solid-State Ionics-2008*; Traversa, E., Armstrong, T. R., Eguchi, K., Palacin, M. R., Eds.; Materials Research Society: Warrendale, PA, 2009; pp 71−78.

(47) Walsh, A.; Watson, G. W.; Payne, D. J.; Edgell, R. G.; Guo, J.; Glans, P.-A.; Learmonth, T.; Smith, K. E. *Phys. Rev. B* **2006**, *73*, 235104.

(48) Mohn, C. E.; Stolen, S.; Norberg, S. T.; Hull, S. *Phys. Rev. Lett.* **2009**, *102*.

(49) Hull, S.; Norberg, S. T.; Tucker, M. G.; Eriksson, S. G.; Mohn, C. E.; Stolen, S. *Dalton Trans.* **2009**, 8737−8745.

(50) An exception to this is cubic δ-Bi_2O_3, where vacancies have been found to order either along the $\langle 100 \rangle$[47] or the $\langle 110 \rangle$ direction.[48,49] This is, however, a very different system, in which the host cation, Bi, is trivalent and very polarizable.